

WITHDRAWN: Microstructure Evolution and Mechanical Properties of Follow-up Micro-hammer Forging Wire + Arc Additive Manufacturing

Xiaochen Xiong

Wuhan University of Technology

Xunpeng Qin

290360@whut.edu.cn

Wuhan University of Technology <https://orcid.org/0000-0001-7656-3748>

Lin Hua

Wuhan University of Technology

Zeqi Hu

Wuhan University of Technology

Shiming Yang

Wuhan University of Technology

Mao Ni

Wuhan University of Technology

Research Article

Keywords: Follow-up micro-hammer forging (FMF), Wire arc additive manufacturing (WAAM), Stress-strain state, Refining grain, Mechanical properties

Posted Date: March 23rd, 2022

DOI: <https://doi.org/10.21203/rs.3.rs-1253233/v1>

License:  This work is licensed under a Creative Commons Attribution 4.0 International License. [Read Full License](#)

EDITORIAL NOTE:

The full text of this preprint has been withdrawn by the authors while they make corrections to the work. Therefore, the authors do not wish this work to be cited as a reference. Questions should be directed to the corresponding author.

Abstract

Aiming at mitigating the problem of coarse grains and poor mechanical properties of wire arc additive manufacturing (WAAM), a variant additive and equivalent hybrid manufacturing technology named follow-up micro-hammer forging (FMF) WAAM is proposed. By employing a multi-DOF industrial robot, the hammer head can synchronously follow the welding gun in a close distance, and the high-density micro-hammer forging is carried out on every deposited weld when the temperature is slightly higher than austenite recrystallization temperature. The larger plastic deformation is introduced to the welds with a smaller hammering force at the temperature. The macro and micro influence of the FMF process is investigated by establishing welding synchronously followed by micro-hammer forging plastic deformation thermal-structural coupling finite element analysis (FEA) model and carrying out experiments. The microstructure and fracture surface are analysed by using OM and SEM. The results show that by introducing the FMF process at 980°C, the stress state and microstructure are improved, and the strength of deposited layers increase significantly. The tensile stress is changed to be compressive stress. The grain size decreases gradually from the bottom deposited layer to the top one showing a genetic evolution law from layer to layer, and the top deposited layer grain size is refined from grade 1 to 7 under the combined influence of recrystallization and co-generation crystallization mechanism. The research conclusions can provide some theoretical guidance for the updating and developing of the hybrid additive manufacturing technology.

1. Introduction

Metal additive manufacturing (AM) process is a short-time strong non-equilibrium metallurgical process coupled with multi-physical fields. The microstructure of deposited material is dominated by coarse columnar grains, which results in the poor performance of AM parts [1–6]. Meanwhile, the stress state within deposited layers is extremely complex, which makes the forming accuracy of AM parts difficult to be controlled effectively [5, 7]. Therefore, how to effectively solve the problems of forming accuracy and performance of AM parts is the key to promote the development and application of metal additive manufacturing technology.

By introducing different assisting manufacturing methods based on mechanical force field [8–17], ultrasonic field [18–23], electromagnetic field [24, 25], laser-energy field [26–29] and other types of energy fields [30] to the process of additive manufacturing or post-processing, the hybrid additive manufacturing owns the advantages of the both and can realize the multi-scale control of the AM parts from microstructure, mesoscopic/macroscopic defects to macroscopic forming accuracy and performance. The additive and subtractive hybrid manufacturing technology based on the milling processing method can effectively improve the forming accuracy and surface quality of parts [8–11], while it has no significant effect on the improvement of microstructure and macro-mechanical properties. Nevertheless, the additive and equivalent hybrid manufacturing technology based on the plastic forming equivalent-quantity manufacturing methods, such as rolling, forging, hammering and so on, can improve the microstructure and stress state of deposited layers, so as to realize the effective control on the macro-mechanical properties of AM parts [12–17, 30].

The hammering assisted AM process is an innovative hybrid manufacturing technology proposed in recent years [31]. Currently, there are few research reports on the technology. Since the hammer head size is small and the contacting style between hammer head and workpiece is point contact, the hammering assisted AM process owns more DOFs and can be less restricted by the shape of workpiece, while the contacting style of the widely studied interlayer rolling process is line contact or cylindrical contact. In addition, the effect of hammering process on workpiece is multi-pass discontinuous impact, which is of a very short acting time and a great instant contact force, so the hammering assisted AM process does not need a set of large equipment to provide static pressure up to dozens of kilonewtons, while it is needed by the interlayer rolling process conversely in order to produce enough plastic deformation in deposited layers. Therefore, the hammering assisted AM process can be well combined with multi-DOF industrial robots with limited carrying capacity and has a wider range of application prospect, owning more processing DOFs, so as to meet the forming manufacturing requirements of complex structure parts.

In the existing reports, the hammering assisted processes are all combined with wire arc additive manufacturing (WAAM) by the means of cross collaboration (AM alternates with hammering), namely interlayer hammering process. Jan Roman Honnige et al. [31, 32] employ a six-DOF ABB industrial robot to carry a high-precision pneumatic hammer peening equipment. A small amount of plastic deformation is implanted on the surface of the Ti-6Al-4V deposited layer by interlayer cold hammer peening process. Under the thermal cycling of subsequent deposited layers, a fine grain layer with a greater depth than the plastic deformation layer is obtained under the action of the recrystallization mechanism, and the mechanical properties of deposited material are improved. Xuewei Fang et al. [33] adopt a three-DOF carrier carrying the pneumatic hammering equipment to conduct the multi-pass hammer peening on the deposited layers of 2319 aluminum alloy when the deposited layers are cooled to 50°C after depositing. When the amount of plastic deformation is increased to 50.8%, the grains of the deposited layers are obviously refined, and the grain size is reduced to 1/10 compared with the as-deposited one. Ultimately, the strength of deposited material is significantly improved under the combined effect of grain refinement and high density dislocation caused by cold plastic deformation, however, the plasticity decreases greatly. The authors [34] also carry out related research in previous studies. The hammering process is carried out when the temperature of the deposited weld is no more than the ferrite recrystallization temperature. The amount of plastic deformation is restricted, only existing in the surface of the weld. The average size of grains in the weld surface is reduced obviously, and the strength of the weld is increased overall to some extent. Hammering temperature is a key process parameter for the process. In all the aforementioned studies for the interlayer hammering process, the hammering temperature is at room temperature or lower than the ferrite recrystallization temperature, which results in the type of hammering deformation belonging to cold plastic deformation. The deformation resistance of hammering is high. The amount of single-pass hammering plastic deformation is limited. The depth of plastic deformation layer is small, and the regulation on microstructure of deposited layers only stays in the surface, which results in heterogeneous mechanical properties for deposited layers. Although the problem of insufficient deformation can be solved by carrying out the multi-pass cyclic hammering or increasing the hammering force, there are still some problems, such as the large energy consumption and low manufacturing efficiency. Moreover, the cold forming is easy to cause serious work hardening, which will greatly reduce the plasticity and toughness of deposited material. In order to eliminate work hardening, the subsequent heat treatments must be introduced which will result in a loss of resources and efficiency.

In order to solve the aforementioned problems, a variant additive and equivalent hybrid manufacturing technology named follow-up micro-hammer forging (FMF) WAAM is proposed. By carrying the hammering device with a independent multi-DOF industrial robot, the hammer head of the hammering device can synchronously follow the welding gun in a close distance. The high-density micro-hammer forging can be carried out on every deposited weld when it is at a higher temperature than A_3 line (to form austenite), and the larger plastic deformation can be introduced into the deposited layers since the deformation resistance is lower at a high temperature, which can effectively control the microstructure and macro-mechanical properties of the deposited layers. In this paper, the influence and mechanism of the FMF process on the microstructure and macro-mechanical properties of the deposited material are studied. The relevant research results and conclusions can provide some theoretical guidance for the updating and developing of hybrid additive manufacturing technology.

2. Fundamental Process

2.1 process principle

Figure 1 shows the principle of the FMF-WAAM process. The multi-DOF carrier robot is employed to carry the hammering device and make the hammer head follow the molten pool closely. The high-density micro-hammer forging is carried out on every deposited weld when the temperature is higher than A_3 line.

The FMF process parameters: hammering timing (after the start of welding), t [s]; hammering following distance, L [mm]; hammering height (distance between hammer head tip and weld surface), H [mm]; hammering deformation rate, ε ;

depression of weld l [mm]; hammering frequency, f [HZ]; hammer traveling speed, V [mm s⁻¹]; hammering density, ρ [mm⁻¹]; hammer head shape.

Through coordinating the additive manufacturing robot and the hammering devices carrier robot, the micro-hammer forging intervention timing can be controlled precisely, namely, the following distance between hammer head and welding gun can be controlled precisely. The micro-hammer forging intervention temperature can be controlled by controlling the following distance between the hammer head and welding gun. The hammer traveling speed must be the same as the welding speed (WS) in order to ensure micro-hammer forging intervention temperatures at all points on deposited weld are the same. The process follows the equations below:

$$t = \frac{L}{V} \quad (1)$$

$$\rho = \frac{f}{V}$$

2

$$\varepsilon = \frac{S_1}{S_0} \times 100\%$$

3

Figure 2 shows the cross section model of weld hammering process.

The hammering deformation rate, ε , can be shown as the following equation:

$$\varepsilon = \frac{S_1}{S_0} = \frac{\int_{x_1}^{x_2} f_1(x) - f_2(x) dx}{\int_0^{x_3} f_1(x) dx}$$

4

Whereas, $f_1(x)$, the original weld profile curve; $f_2(x)$, the profile curve of the hammering mark; x_1, x_2 , the x-coordinate of the intersections of $f_1(x)$ and $f_2(x)$; x_3 , the x-coordinate of the endpoint of the original weld profile curve.

2.2 Identification of key process parameters

Figure 3a shows the temperature values of the points on the depositing weld with different distances from the welding gun, namely the temperature of the micro-hammer forging plastic deformation on the weld at different hammering following distance. The temperature values are measured by a thermal imager (Fig. 3b)

According to the theory of thermoplastic forming, the ferrite grain refinement can be realized by plastic deformation both in austenite unrecrystallized temperature zone or recrystallized temperature zone. However, the plastic deformation resistance is larger in austenite unrecrystallized temperature zone than recrystallized temperature zone, and the higher force and energy is required to produce a certain amount of plastic deformation. What's more, it is easier to cause hot work hardening in austenite unrecrystallized temperature zone, which will result in the plasticity of the deposited layers decreasing. Therefore, the micro-hammer forging plastic deformation on deposited weld at a temperature higher than austenite recrystallization temperature is worthy to be studied deeply. The austenite recrystallization temperature of low carbon low alloy steel is about 950°C. When the plastic deformation temperature is too high, the austenite grains are easy to coarsening, which is not conducive to obtaining the fine ferrite structure after transformation. In addition, to protect the hammer head and prevent interference, the minimum following distance between the hammer head and the welding gun should be greater than 20mm, so the two temperatures, 980°C and 1080°C, are selected for study (the following distances between the hammer head to welding gun are about 30mm and 25mm).

Figure 4a and b show the metallographic diagrams of weld surfaces which are processed by the follow-up micro-hammer forging process to the same amount of plastic deformation at the temperature of 980°C and 1080°C. As shown in Fig. 4 the finer average grain size is obtained at 980°C than at 1080°C. Compared with 980°C, the grains obtained at 1080°C tend to coarsen. Therefore, the temperature 980°C, slightly higher than the austenite recrystallization temperature, is finally chosen to carry out the follow-up micro-hammer forging process. The hammering intervention timing is about 5s after the start of welding according to the Eq. (1).

In order to obtain relatively uniform microstructure of weld and retain the characteristics of additive manufacturing, the hammer plastic deformation, ϵ , is determined to be about 40%, and by substituting it into Eq. (4), the depression of weld l is determined to be about 1.5mm.

3. Finite Element Simulation (Fem)

The FMF finite element simulation model is established to analyze the influence of FMF on the stress-strain state of deposited weld, which determines the microstructure of the weld.

The simulation parameters are set as the same with experimental: the following distance between the hammer head and welding gun, 30mm; the hammer traveling speed, 6mm/s; the hammering frequency, 27Hz; the hammering density (ρ), 4.5/mm.

Figure 5a shows the distribution of the maximum principal stress in the weld zone and heat-affected zone (HAZ) when the deposited weld is cooled directly to room temperature after depositing. Fig. 5b is for the FMF group, the weld is also cooled to room temperature after the FMF process. As shown in Fig. 5a, for the as-deposited group, the middle of the weld zone and the HAZ on both sides of the weld both show a state of tensile stress, and the value of the tensile stress on both sides of the HAZ is larger than that of the middle of the weld zone. Nevertheless, in Fig. 5b, the weld zone processed by the FMF presents a state of compressive stress on the whole, and the HAZ on both sides of the weld presents a state of tensile stress. However, the stress values in the HAZ on both sides of the weld is significantly reduced compared with that of the as-deposited group (Fig. 6). The above results reveal that under the effect of FMF process, the stress state of the weld zone can be changed from tensile stress state to compressive, and the tensile stress of the HAZ on both sides of the weld can be reduced to some extent.

Figure 7a is the equivalent strain distribution of central cross section of the deformed weld processed by high-density micro-hammer forging in Fig. 5b, while Fig. 7b is for single-point micro-hammer forging. Make the cross section deformation rate ($\dot{\epsilon}$) of single-point micro-hammer forging similar to that of the high-density micro-hammer forging (the single-point micro-hammer forging needs higher hammering speed). The results show that there are some differences in strain distribution between the two. For the weld cross section of single-point micro-hammer forging, the region close to the middle of the hammering mark is hard deformation zone. The two sides and lower part of the region are large deformation zone. However, for the cross section of the high-density micro-hammer forging, the region close to the middle of the hammering mark is super deformation zone. The two sides and lower part of the region are large deformation zone, and the lower part is small deformation zone. The high-density micro-hammer forging makes the metal in the original hard deformation zone (for the single-point micro-hammer forging) undergo repeatedly deformation. The hard deformation zone turns into a super deformation zone, which breaks the law of the single-point plastic deformation. Nevertheless, the speed of each point of multi-point high-density micro-hammer forging does not need to be as high as the single-point micro-hammer forging. The large plastic deformation is formed by accumulation of multi-point high-density small plastic deformation which can be understood from the view of energy input. The equivalent strain characteristics of the weld correspond to the microstructure and mechanical properties.

4. Experimental Procedure

As shown in Fig. 8, the experiments are carried out on the FMF-WAAM experiment system composed of a WAAM module, a FMF module and a worktable. The FMF module is mainly composed of a multi-DOF YASAWA robot, a set of parameter-variable electric hammering device refitted from an electric pick, a spherical hammer head with a diameter of 15mm, and a fixture to attach the hammering device to the carrier robot.

The welding material for WAAM is AWS ER70S-6. The chemical composition of the material is shown in the Table 1. The substrate is AISI 1045.

Table 1
Chemical composition of AWS ER70S-6 (wt %).

| Material | C | Si | Mn | Cr | Ni | P | S | Mo | V | Cu |
|-------------|-----------|-----------|-----------|-------|-------|--------|--------|-------|-------|-------|
| AWS ER70S-6 | 0.06~0.15 | 0.08~1.15 | 1.40~1.85 | ≤0.15 | ≤0.15 | ≤0.025 | ≤0.025 | ≤0.15 | ≤0.03 | ≤0.50 |

The FMF process is started at the same time with welding. The hammer head is located in the middle of the deposited weld. The hammer head moves synchronously with the welding gun at the same speed. The WAAM and FWM parameters are shown in the Table 2

Table 2
WAAM and FWM experiment parameters.

| Parameter | Value |
|---------------------------------------|-----------------------|
| Welding voltage | 24V |
| Welding speed | 6mm/s |
| Wire feeding speed | 6.5m/min |
| Welding wire diameter | 1.2mm |
| Hammering following distance | 30mm |
| Input voltage of the hammering device | 105-110V |
| Maximum hammering speed | 2.47m/s |
| Hammering frequency | 27-28Hz |
| Hammering density | 4.5/mm |
| Hammer head shape | Spherical hammer head |
| Hammering deformation rate | About 40% |
| Depression of weld | About 1.5mm |

Figure 9 shows the deposited layers of single-layer single-pass (Figure 9a) and three-layer ten-pass (Figure 9b) manufactured by the FMF-WAAM process. The samples of metallographic analyses and tensile tests are cut from the block shown in Figure 9b.

The metallographic samples are cut by wire cutting. After mechanical grinding and polishing, they are etched with low-concentration picric acid aqueous solution at 65-70°C for 30s. Then the metallography is observed by optical microscope. The tensile sample dimensions is shown in Fig. 10.

5. Results And Discussion

5.1 Microstructure

Figure 11a and b show the cross sections of single-layer single-pass deposited weld of the as-deposited group and the FMF one.

Figure 12a and b show the metallographic diagrams of Fig. 11a and b. As shown in Figure 12a, the section of as-deposited group is dominated by coarse columnar grains with a grain size about grade 1. Most of the columnar grains start from the solid-liquid crystal interface, develop perpendicular to the fusion line, and finally run through the entire weld zone to the surface of the weld. The grain morphology is formed by grains nucleating on the surface of base metal and growing perpendicularly to the isothermal surface of the fusion line under the condition of high superheating temperature and high temperature gradient. As shown in Fig. 12b, the two different morphologies equiaxed grains and columnar grains are distributed in the cross section of the FMF group with a grain size about grade 4. The proportion and size of columnar grains decrease significantly compared with the as-deposited one. The cross section of the FMF group is dominated by relatively small columnar grains and equiaxed grains. The reason why the grain morphology of FMF group is different from that of the as-deposited one is that along with high-density micro-hammer forging under the high temperature about 980°C, the metal in the weld zone undergoes a large degree of plastic deformation (the deformation rate is about 40%). Since the temperature during the deformation is higher than the austenite recrystallization temperature, the austenite dynamic recrystallization will occur during the deformation process, and the static recrystallization will gradually occur along with the temperature decreasing after deformation in the weld zone. Due to the limited degree of plastic deformation in small deformation zones during the whole process, the deformation energy storage is relatively limited. In addition, because the size of the deposited weld to substrate is approximately infinitesimal, the thermal conductivity coefficient in the welding heat dissipation process is high. The cooling rate of the metal in the weld zone is very high. The activity and diffusion ability of metal atoms show a sharp downward trend. Therefore, the proportion of austenite recrystallization in the deformed weld zone is limited to some extent, resulting in uneven austenite recrystallization. Ultimately, as the austenite transforms into ferrite, the coexistence of the fined equiaxed grains, plastically deformed broken columnar grains and original as-deposited columnar grains appears.

Figure 13a and b are the cross sections of the cutted three-layer three-pass deposited layers of the as-deposited group and the FMF one.

Figure 14a-f show the metallographic diagrams of Fig. 13a and b. Specifically, Fig. 14a and b are the regions near the lower edge of the first pass weld in the first deposited layer (the bottom deposited layer). Fig. 14a is for the as-deposited group, and Fig. 14b is for the FWM one. As shown in Fig. 14a and b, the weld cross section of as-deposited group is dominated by columnar grains, while that of the FMF one is dominated by equiaxed grains and a few of columnar grains. By comparing the grain morphologies and sizes of the two groups, it is found that the grain size of the FMF group is significantly reduced, and the grain refinement effect is significant. Besides the uneven austenite recrystallization in the processes of the high-density hammering thermoplastic deformation and weld cooling, there is another reason for the grain refinement of FMF group. Specifically, the repeated thermal cycles of the subsequent deposited welds on the deformed welds increase the metal atom activity in the previous deformed zone with incomplete recrystallization, which makes the metal atoms of the zone obtain sufficient diffusion ability. Meanwhile, the high-density hammering thermoplastic deformation on the subsequent deposited welds will make further plastic deformation in the previous deformed welds. Therefore, the continuous recrystallization behavior of the previous deformed welds will occur. Ultimately, the proportion of metal recrystallization in the deformation zone is increased, which results in the further grain refinement in the previous deformed welds.

Figure 14c and d are the junctional regions between the first pass weld of the first deposited layer and that of the second deposited layer. The lower parts of Figure 14c and d are the regions near the core of the first-layer weld, and the upper parts are the fusion zone and surrounding regions of the second-layer weld. The Figure 14c for the as-deposited group of which

the lower part is distributed with the coarse columnar grains and upper part with the slender size of columnar grains, while the Fig. 14d for the FMF one of which the lower part is dominated by large size equiaxed grains and a few of small size columnar grains and upper part with fine equiaxed grains and a few of fine columnar grains. Figure 14c for the as-deposited group, the coarse columnar grains in the lower part are caused by the serious overheating of the weld core which reduces the number of original particles. What's more, the small constitutional supercooling of the final cooling zone in the weld core is another reason, which reduces the nucleation rate of grains and generates the coarse columnar grains. However, Fig. 14d for the FMF one, the large size equiaxed grains and a few of fine columnar grains in the lower part are due to the austenite recrystallizing during and after the process of high-density micro-hammer forging on the previous deposited weld and the static recrystallization under the action of thermal cycles of the subsequent deposited welds. Because the original grain size of the weld core is large, the grain size after recrystallization is also large. What's more, the weld core is seriously overheated and the recrystallized austenite grain is easy to coarsen. Ultimately, the large size equiaxed grains coexist with the small size columnar grains in the FMF group. Figure 14c for the as-deposited group, the elongated columnar grains in the upper part are due to the high cooling rate which results in a larger degree of supercooling near the solid-liquid interface in the fusion zone and the regions nearby. However, Fig. 14d for the FMF one, the reasons for the formation of fine size equiaxed grains and a few of fine size columnar grains in the upper part are as follows. The austenite recrystallization occurs during and after the process of hammering thermoplastic deformation in the welds. In addition, the deformed welds recrystallize under the action of thermal cycles of the subsequent deposited welds. What's more, there is another major reason. Specifically, along with the austenite recrystallization occurring during and after the hammering thermoplastic deformation, the refined grains are obtained in the previous deposited weld (the first-layer weld). The molten pool crystal interface of subsequent deposited weld attaches to the surface of the previous grain-refined deposited weld to produce co-crystallization. Therefore, the grain size of the subsequent deposited weld is reduced and the grains with refinement structure are obtained.

Figure 14e and f are the regions near the surface of the first pass weld in the top deposited layer (the third deposited layer). Figure 14e for the as-deposited group, where there are a large number of large-size columnar grains and an extremely thin equiaxed fine grain layer on the surface of the weld with a grain size about grade 1. However, Fig. 14f for the FMF group, the fine size equiaxed grains are uniformly distributed with a grain size about grade 7. Besides the reason that austenite recrystallization occurs in the metal with super plastic deformation close to the middle of the hammering mark (as shown in FEM simulation results) during and after the process of hammering plastic deformation, there is another major reason. The grain sizes of the deposited layers from the bottom layer to the top one have a genetic tendency under the influence of the high-density micro-hammer forging and the mechanism of co-generation crystallization nucleation. Ultimately, the deposited layers are refined layer by layer, and the grain size of the top deposited layer is greatly reduced. The top deposited layer with remarkable grain refinement effect is finally obtained.

Figure 15a-d are also the metallographic diagrams of Fig. 13a and b for the as-deposited group and the FMF one. Specifically, Fig. 15a and b show the lap bonding regions between the first pass weld and the second one in the bottom deposited layer (the first deposited layer). Fig. 15a for the as-deposited group is all distributed with the coarse columnar grains, while Fig. 15b for the FMF one is dominant by equiaxed grains with smaller size, except for a very small quantity of fine-sized columnar grains near the border line. In addition, the size of equiaxed grains near the next weld fusion line increases slightly. For the welds processed by high-density micro-hammer forging, the lap bonding region between the two welds also undergoes plastic deformation to some degree and is a large deformation zone (as shown in FEM simulation results). The recrystallization will occur during the thermoplastic deformation, in the phase of weld cooling and thermal cycles of the subsequent deposited welds. Therefore, the deposited material with refined grains can be obtained. The size of equiaxed grains increasing near the fusion line of the next weld is due to the coarsening of recrystallized grains after overheating by thermal cycles of the subsequent deposited welds.

Fig. 15c and d show the lap bonding regions between the first pass weld and the second one in the top deposited layer (the third deposited layer). The Fig. 15c for the as-deposited group is similar to that of Fig. 15a. The whole region are distributed

with columnar grains with large size. Fig. 15d for the FMF one, the fine-size equiaxed grains are uniformly distributed in the lap bonding region of the two welds, and the grain size is finer and smaller than that in Fig. 15b. The reason for the significant change of grain morphology and size of the FMF group compared with the as-deposited one is similar to that in the lap bonding region of the two welds in the first deposited layer. Nevertheless, there are two aspects of reasons why the finer and smaller grains can be obtained than those in the lap bonding region of the two welds in the bottom deposited layer (the first deposited layer). Firstly, the top deposited layer recrystallized grain refined by high-density micro-hammer forging does not have a subsequent deposited layer to melt the surface fine grain layer, but the bottom deposited layer does. Secondly, the grain-refined deposited layer after deformation has genetic evolution influence on the grain size of the subsequent deposited layers from the bottom layer to the top one after deformation through the co-generation crystallization mechanism, which is conducive to obtain the finer equiaxed grains on the top deposited layer.

5.2 Mechanical properties

5.2.1 Hardness

Figure 16 shows the hardness values of each deposited layer of the as-deposited group and the FMF one. Measuring way: Each deposited layer is divided into three regions bottom-up. Specifically, the region near the fusion line at the bottom of the deposited layer, the central region of the deposited layer and the upper region of the deposited layer (not the surface). Each region at least 5-10 testing points are selected, and not less than 20 testing points are tested in each deposited layer. Finally, the average value of the measured data points in the three regions is used as the hardness value of the deposited layer.

As shown in Fig. 16, the hardness values of the FMF deposited layers are improved compared with those of the as-deposited one. The improvement ranges are 22.9% for the first deposited layer (the bottom deposited layer), 25% for the second deposited layer, and 33.6% for the third deposited layer (the top deposited layer). In addition, for the as-deposited group, the hardness of each deposited layer gradually decreases from the bottom to the top, while for the FMF one, the hardness of each deposited layer gradually increases from the bottom to the top. The reason may be related to the genetic evolution of the grain size of each deposited layer from the bottom to the top as previously found.

5.2.2 Strength

Figure 17a-d show the stress-strain curves of longitudinal and transverse samples for the as-deposited group and the FMF one, and the relevant results are shown in Fig. 18. Compared with the as-deposited group, the longitudinal and the transverse strength of the FMF one are greatly improved. The longitudinal tensile strength is increased from 570.1MPa to 665.1MPa by 16.7%, the yield strength is increased from 445.3MPa to 581.2MPa by 30.5%. The transverse tensile strength is increased from 566.9MPa to 671.9MPa by 18.5%, the yield strength is increased from 443.8MPa to 584.5MPa by 31.7%. Nevertheless, the longitudinal ductility decreases slightly from 33.5–29.85%, and the transverse ductility decreases from 30.1–25.7%, but it still shows the good plasticity.

The enhancing mechanism of FWM to deposited layers has two aspects. Firstly, the high-density micro-hammer forging makes the deposited layers undergo thermoplastic deformation, which makes the stress state of the deposited layers change from unfavorable tensile stress to favorable compressive stress. Although the thermoplastic deformation is accompanied by high temperature softening, the high density deformation dislocation is still left in the deposited layers after cooling to achieve dislocation strengthening. Secondly, the recrystallization occurs during the thermoplastic deformation, in the phase of weld cooling and thermal cycles of the subsequent deposited welds. Therefore, the deposited material with refined grains can be obtained which will achieve fine grains strengthening.

In addition, the longitudinal and the transverse strength and ductility of both groups are slightly different. For the as-deposited group, the longitudinal strength and ductility are slightly higher than that of the transverse ones, while for the FMF one, the longitudinal strength but ductility are slightly lower than that of the transverse ones. However, the anisotropy is not obvious on the whole. The main reason for the differences between the longitudinal and the transverse of the FMF

group is that the sampling positions of the longitudinal samples are random, which might be the super and large deformation zone near the middle of the hammering mark or the small deformation zone on both sides of the hammering mark. Therefore, the test results are scattered, and the mean strength of the longitudinal results is slightly smaller than that of the transverse one, while the mean ductility is higher than that of the transverse one.

Figure 19 shows the SEM images and local enlarged views of fracture surfaces of the longitudinal and the transverse tensile samples of the as-deposited group and the FMF one. Figure 19a and b show the longitudinal tensile fracture surfaces of the as-deposited group, while Figure 19c and d show those of the FMF one. Figure 19e and f show the transverse tensile fracture surfaces of the as-deposited group, while Figure 19g and h show those of the FMF one. Compared with the FMF group, the as-deposited longitudinal tensile fracture surface is relatively flat, and equiaxial dimples of uniform size are distributed in the local amplification region, which is the typical ductile fracture characteristic of micropore aggregation. However, the flatness of the fracture surface of the FMF group is poor. The degree of fluctuation of the fracture surface is large, and a large number of dimples formed by microporous aggregated ductile fracture are also found in the fracture surface after local magnification. Nevertheless, the dimples are relatively small in size, and the distribution is denser. What's more, the distribution fluctuation in the fracture surface is larger. Comparing the transverse tensile fracture surface of the as-deposited group with the FMF one, the as-deposited group is relatively flat, while the fluctuation of the FMF one is larger. The local amplification regions of the transverse tensile fracture surface of the as-deposited group and the FMF one are similar to the longitudinal tensile fracture surface of the two. The uniform size of equiaxial dimples is distributed in the as-deposited group, while the dimples of the FMF group are smaller than that of the as-deposited one, and the distribution is denser and slightly undulating. This is also the reason why the hardness and strength of the samples in the FMF group are greatly improved compared with those of the as-deposited one, while the ductility is reduced to some extent.

6. Conclusion

The experimental and analytical results show that the FMF process can improve the mechanical properties of the low carbon low alloy steel deposited layers. The relevant conclusions are as follows:

- (1) The follow-up micro-hammer forging (FMF) process, by introducing a large degree of plastic deformation to the deposited weld at the temperature slightly higher than the austenite recrystallized temperature, the stress state of tensile stress of the deposited weld can be changed to compressive stress, and the tensile stress of the HAZ on both sides of the weld can be reduced significantly.
- (2) The plastic deformation at the temperature slightly higher than austenite recrystallization temperature can promote the austenite recrystallization of the metal in the deposited layers, which can greatly reduce the grain size of each deposited layers significantly, while the grains will coarsen at higher temperature.
- (3) Due to the recrystallization grain refinement by high-density thermoplastic deformation and the interfacial co-generation crystallization mechanism, the grain sizes of the deposited layers have a genetic evolution law, and the grain size of each deposited layer gradually decreases from the bottom layer to the top one. Finally, the grain size of the top deposited layer is refined from grade 1 to grade 7.
- (4) The FMF process can increase the hardness and strength of the deposited layers, but will decrease the plasticity to some degree. However, the deposited material still shows a good plasticity.

Declarations

Availability of data and materials

The datasets supporting the conclusions of this article are included within the article.

Competing interests

The authors declare no competing financial interests.

Funding

This work is financially supported by the Key Technologies Research and Development Program of China (2018YFB1106500), the Technical Innovation Special Project of Hubei Province (2020BED010), the Technical Innovation Special Project of Hubei Province (2019AAA075) and the Innovative Research Team Development Program of Ministry of Education of China (No. IRT17R83).

Authors' contributions

The author' contributions are as follows: Xunpeng Qin and Lin Hua were in charge of the whole trial; Xiaochen Xiong wrote the manuscript; Zeqi Hu, Shiming Yang and Mao Ni assisted with sampling and laboratory analyses.

Acknowledgements

Not applicable

Consent for publication

Not applicable

Ethics approval and consent to participate

Not applicable

References

1. G. Marinelli, F. Martina, S. Ganguly, S. Williams, Grain refinement in an unalloyed tantalum structure by combining Wire+Arc additive manufacturing and transverse cold rolling, *Additive Manufacturing* 32 (2020).
2. J. Donoghue, A.E. Davis, C.S. Daniel, A. Garner, F. Martina, J. Quinta da Fonseca, P.B. Prangnell, On the observation of annealing twins during simulating β -grain refinement in Ti-6Al-4V high deposition rate AM with in-process deformation, *Acta Materialia* 186 (2020) 229–241.
3. A.E. Davis, J.R. Hönnige, F. Martina, P.B. Prangnell, Quantification of strain fields and grain refinement in Ti-6Al-4V inter-pass rolled wire-arc AM by EBSD misorientation analysis, *Materials Characterization* 170 (2020).
4. P. Dryburgh, D. Pieris, F. Martina, R. Patel, S. Sharples, W. Li, A.T. Clare, S. Williams, R.J. Smith, Spatially resolved acoustic spectroscopy for integrity assessment in wire-arc additive manufacturing, *Additive Manufacturing* 28 (2019) 236–251.
5. J.R. Hönnige, P.A. Colegrove, S. Ganguly, E. Eimer, S. Kabra, S. Williams, Control of residual stress and distortion in aluminium wire + arc additive manufacture with rolling, *Additive Manufacturing* 22 (2018) 775–783.
6. X. Zhang, F. Martina, J. Ding, X. Wang, S.W. Williams, Fracture toughness and fatigue crack growth rate properties in wire + arc additive manufactured Ti-6Al-4V, *Fatigue & Fracture of Engineering Materials & Structures* 40(5) (2017) 790–803.
7. R. Li, J. Xiong, Y. Lei, Investigation on thermal stress evolution induced by wire and arc additive manufacturing for circular thin-walled parts, *Journal of Manufacturing Processes* 40 (2019) 59–67.

8. K.P. Karunakaran, S. Suryakumar, V. Pushpa, S. Akula, Low cost integration of additive and subtractive processes for hybrid layered manufacturing, *Robotics and Computer-Integrated Manufacturing* 26(5) (2010) 490–499.
9. Q. Bai, B. Wu, X. Qiu, B. Zhang, J. Chen, Experimental study on additive/subtractive hybrid manufacturing of 6511 steel: process optimization and machining characteristics, *The International Journal of Advanced Manufacturing Technology* 108(5-6) (2020) 1389–1398.
10. K. Salonitis, L. D’Alvise, B. Schoinochoritis, D. Chantzis, Additive manufacturing and post-processing simulation: laser cladding followed by high speed machining, *The International Journal of Advanced Manufacturing Technology* 85(9-12) (2015) 2401–2411.
11. X. Xiong, H. Zhang, G. Wang, Metal direct prototyping by using hybrid plasma deposition and milling, *Journal of Materials Processing Technology* 209(1) (2009) 124–130.
12. C. Hopper, C.I. Pruncu, P.A. Hooper, Z. Tan, S.T. Yang, Y. Liu, J. Jiang, The effects of hot forging on the preform additive manufactured 316 stainless steel parts, *Micron* 143 (2021) 103026.
13. J. Ma, Y. Zhang, J. Li, D. Cui, Z. Wang, J. Wang, Microstructure and mechanical properties of forging-additive hybrid manufactured Ti–6Al–4V alloys, *Materials Science and Engineering: A* 811 (2021).
14. P.A. Colegrove, H.E. Coules, J. Fairman, F. Martina, T. Kashoob, H. Mamash, L.D. Cozzolino, Microstructure and residual stress improvement in wire and arc additively manufactured parts through high-pressure rolling, *Journal of Materials Processing Technology* 213(10) (2013) 1782–1791.
15. J.R. Hönnige, P.A. Colegrove, B. Ahmad, M.E. Fitzpatrick, S. Ganguly, T.L. Lee, S.W. Williams, Residual stress and texture control in Ti-6Al-4V wire + arc additively manufactured intersections by stress relief and rolling, *Materials & Design* 150 (2018) 193–205.
16. A.R. McAndrew, M. Alvarez Rosales, P.A. Colegrove, J.R. Hönnige, A. Ho, R. Fayolle, K. Eytayo, I. Stan, P. Sukrongpang, A. Crochemore, Z. Pinter, Interpass rolling of Ti-6Al-4V wire + arc additively manufactured features for microstructural refinement, *Additive Manufacturing* 21 (2018) 340–349.
17. Y. Fu, H. Zhang, G. Wang, H. Wang, Investigation of mechanical properties for hybrid deposition and micro-rolling of bainite steel, *Journal of Materials Processing Technology* 250 (2017) 220–227.
18. C. Zhou, J. Wang, C. Guo, C. Zhao, G. Jiang, T. Dong, F. Jiang, Numerical study of the ultrasonic impact on additive manufactured parts, *International Journal of Mechanical Sciences*, 197 (2021).
19. Y. Tian, J. Shen, S. Hu, J. Han, Q. Wang, Y. Cai, Effects of ultrasonic peening treatment layer by layer on microstructure of components fabricated by wire and arc additive manufacturing, *Materials Letters* 284 (2021).
20. A.I. Gorunov, Additive manufacturing of Ti6Al4V parts using ultrasonic assisted direct energy deposition, *Journal of Manufacturing Processes* 59 (2020) 545–556.
21. H. Wang, Y. Hu, F. Ning, W. Cong, Ultrasonic vibration-assisted laser engineered net shaping of Inconel 718 parts: Effects of ultrasonic frequency on microstructural and mechanical properties, *Journal of Materials Processing Technology* 276 (2020).
22. D. Yuan, S. Shao, C. Guo, F. Jiang, J. Wang, Grain refining of Ti-6Al-4V alloy fabricated by laser and wire additive manufacturing assisted with ultrasonic vibration, *Ultrason Sonochem* 73 (2021) 105472.
23. D. Zhang, Y. Li, H. Wang, W. Cong, Ultrasonic vibration-assisted laser directed energy deposition in-situ synthesis of NiTi alloys: Effects on microstructure and mechanical properties, *Journal of Manufacturing Processes* 60 (2020) 328–339.
24. X. Bai, H. Zhang, Z. Xiangman, G. Wang, Electromagneto-fluid Coupling Simulation of Arc Rapid Prototyping Process with External High-frequency Magnetic Field, *Journal of Mechanical Engineering* 52 (2016) 60–66 and 72.
25. X.W. Bai, H.O. Zhang, G.L. Wang, Electromagnetically Confined Weld-based Additive Manufacturing, *Procedia CIRP* 6 (2013) 515–520.
26. J. Chi, Z. Cai, H. Zhang, H. Zhang, W. Guo, Z. Wan, G. Han, P. Peng, Z. Zeng, Combining manufacturing of titanium alloy through direct energy deposition and laser shock peening processes, *Materials & Design* 203 (2021).

27. N. Kalentics, M.O.V. de Seijas, S. Griffiths, C. Leinenbach, R.E. Logé, 3D laser shock peening – A new method for improving fatigue properties of selective laser melted parts, *Additive Manufacturing* 33 (2020).
28. N. Navin Kumar, A. Chandrakant Yadav, K. Raja, C.D. Naiju, S. Prabhakaran, S. Kalainathan, Laser Shock Peening on Al-Si10-Mg Produced by DMLS Technique, *Materials Today: Proceedings* 22 (2020) 2916-2925.
29. Z. Tong, H. Liu, J. Jiao, W. Zhou, Y. Yang, X. Ren, Microstructure, microhardness and residual stress of laser additive manufactured CoCrFeMnNi high-entropy alloy subjected to laser shock peening, *Journal of Materials Processing Technology* 285 (2020).
30. K.A. Shiyas, R. Ramanujam, A review on post processing techniques of additively manufactured metal parts for improving the material properties, *Materials Today: Proceedings* (2021).
31. J.R. Hönnige, P.A. Colegrove, S.W. Williams, Wire + Arc Additively Manufactured Ti-6Al-4V with Machine Hammer Peening, *Procedia Engineering* 216 (2017) 8–17.
32. J.R. Hönnige, A.E. Davis, A. Ho, J.R. Kennedy, L. Neto, P. Prangnell, S. Williams, The Effectiveness of Grain Refinement by Machine Hammer Peening in High Deposition Rate Wire-Arc AM Ti-6Al-4V, *Metallurgical and Materials Transactions A* 51(7) (2020) 3692–3703.
33. X. Fang, L. Zhang, G. Chen, K. Huang, F. Xue, L. Wang, J. Zhao, B. Lu, Microstructure evolution of wire-arc additively manufactured 2319 aluminum alloy with interlayer hammering, *Materials Science and Engineering: A* 800 (2021).
34. X. Xiong, X. Qin, F. Ji, Z. Hu, L. Hua, Microstructure and Mechanical Properties of Wire + Arc Additively Manufactured Mild Steel by Welding with Trailing Hammer Peening, *steel research international* (2021).

Figures

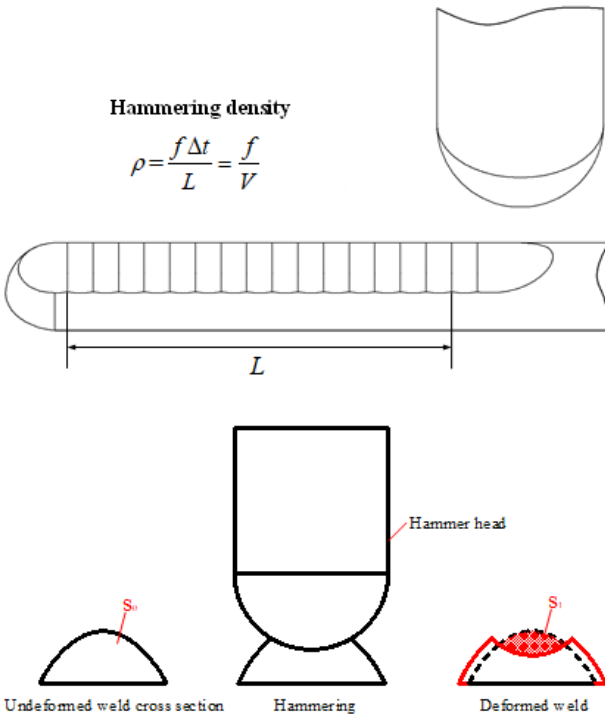
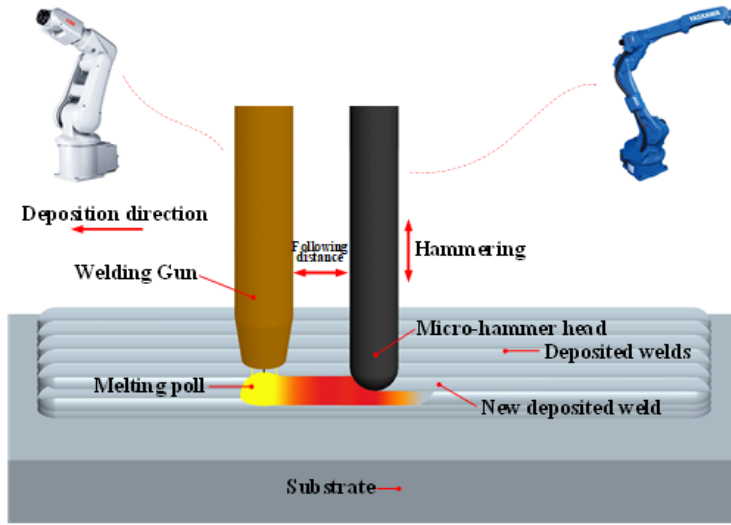


Figure 1

Process principle of the FMF-WAAM

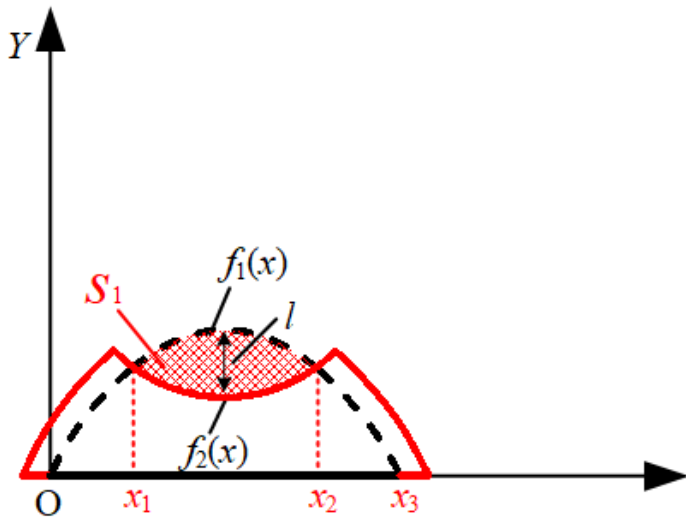


Figure 2

Plane model of weld micro-hammer forging.

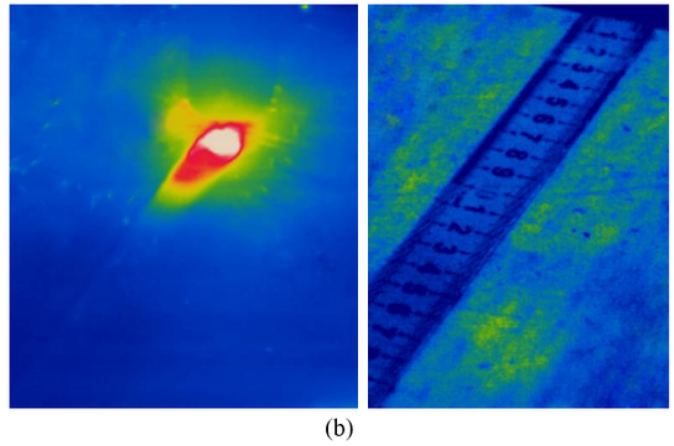
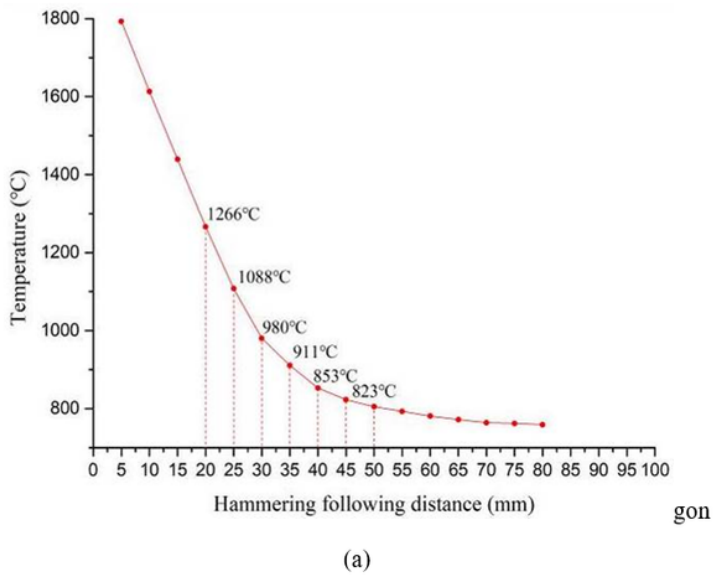


Figure 3

Temperature values of micro-hammer forging plastic deformation with different following distances: (a) temperature values of the points on the depositing weld with different distances from the welding gun; (b) employing a thermal imager measuring the temperature values

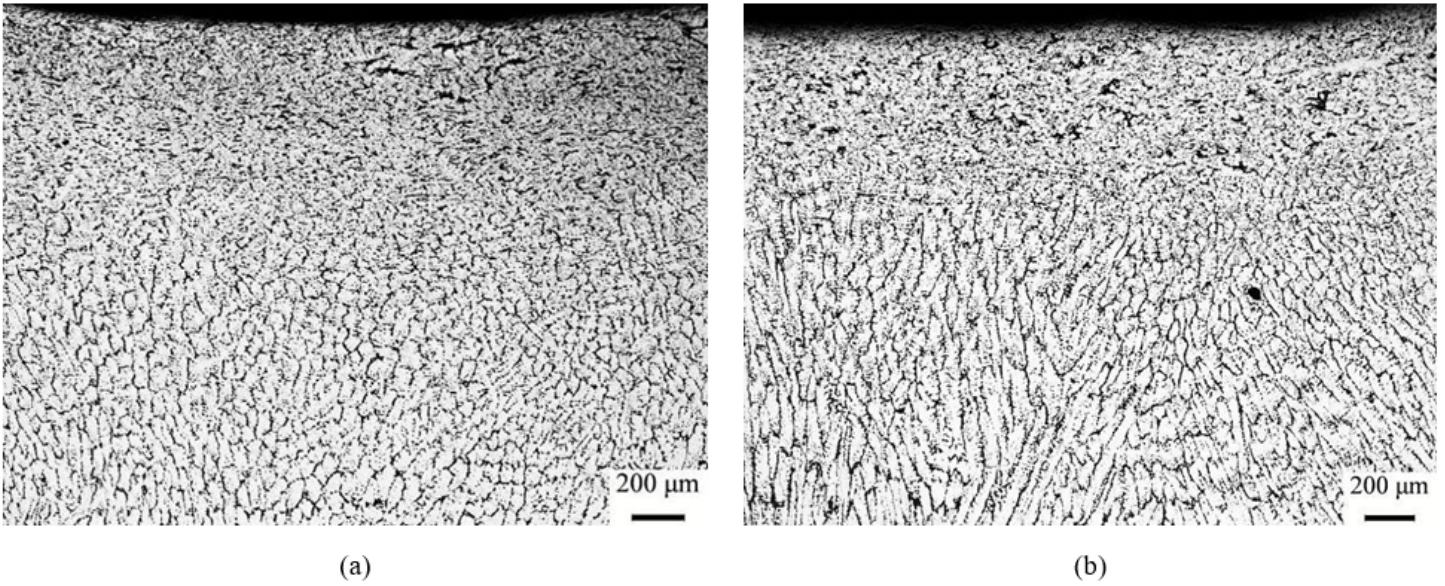


Figure 4

metallographic diagrams of weld surfaces by the follow-up micro-hammer forging process: (a) at 980°C; (b) at 1080°C

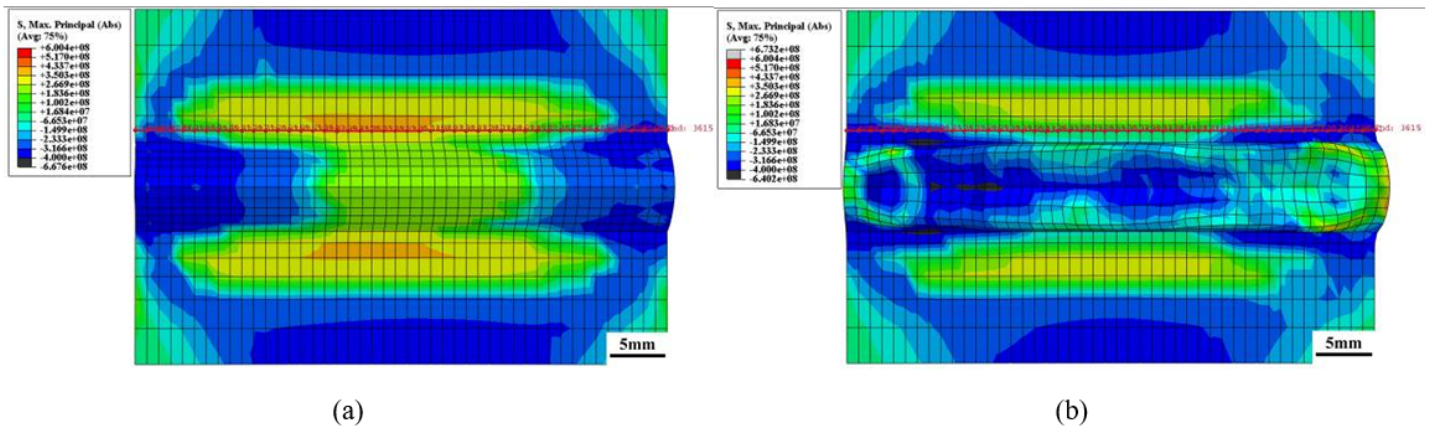


Figure 5

Distribution of the maximum principal stress in the weld zone: (a) as-deposited; (b) FME.

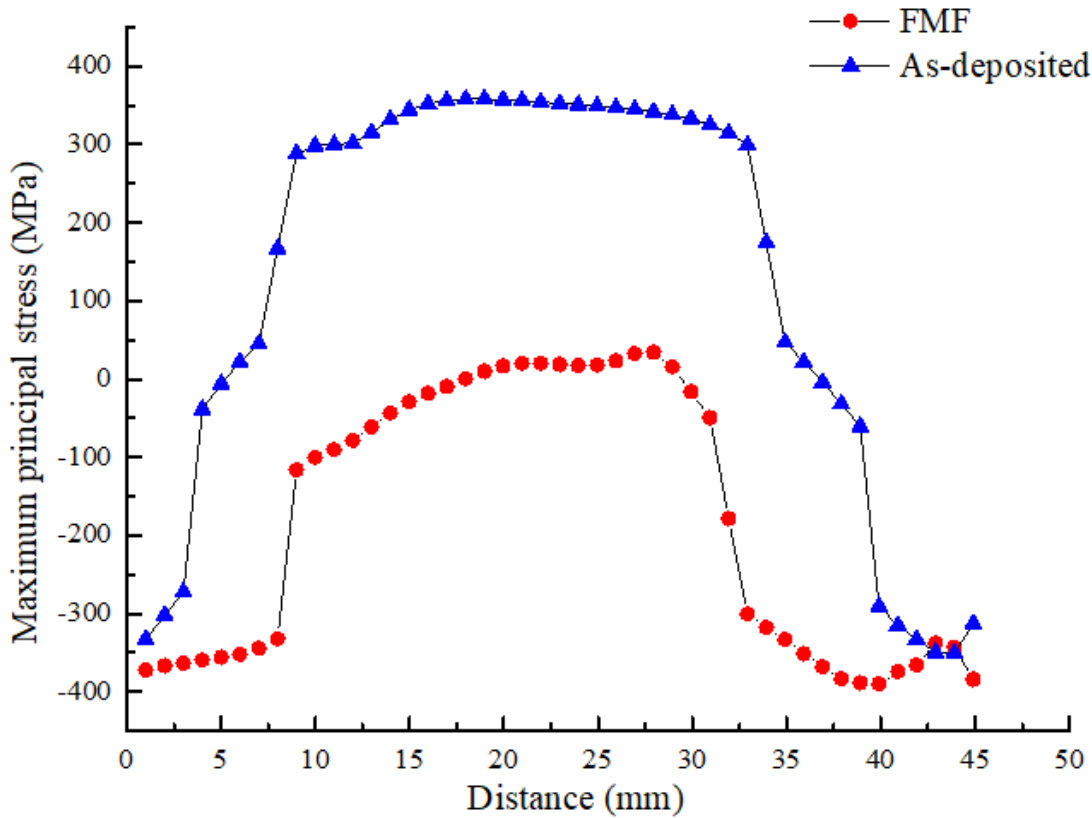


Figure 6

Distribution of the maximum principal stress of the selected path in the weld zone of the as-deposited group and the FMF one in Fig. 5.

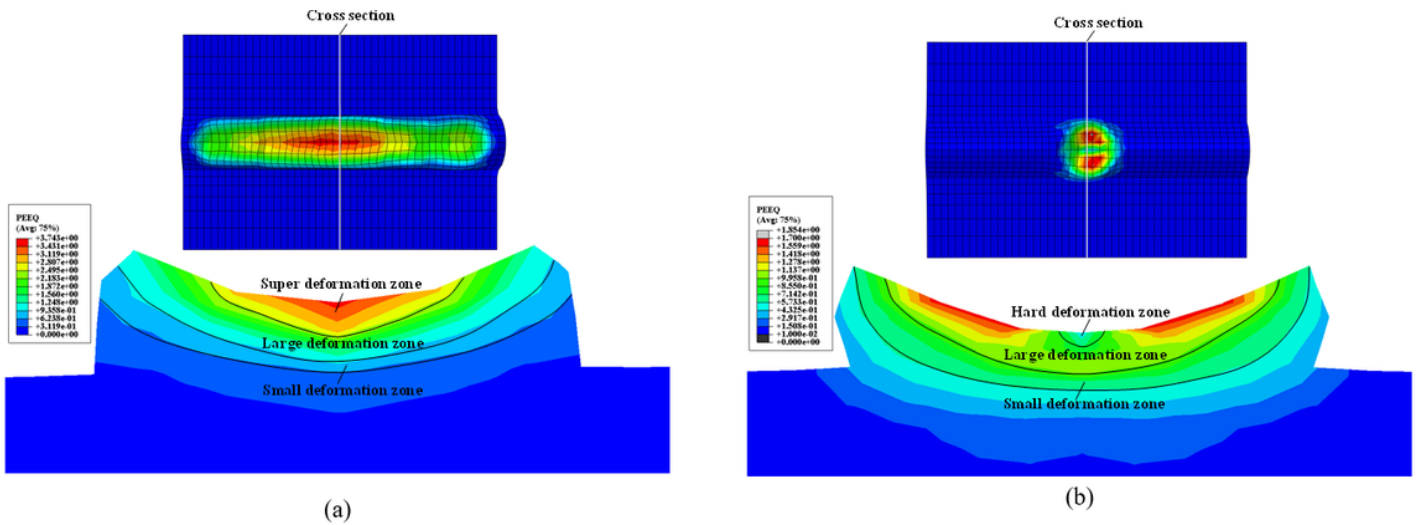


Figure 7

Equivalent strain distribution of central cross section of deformed weld: (a) high-density micro-hammer forging; (b) single-pass micro-hammer forging.

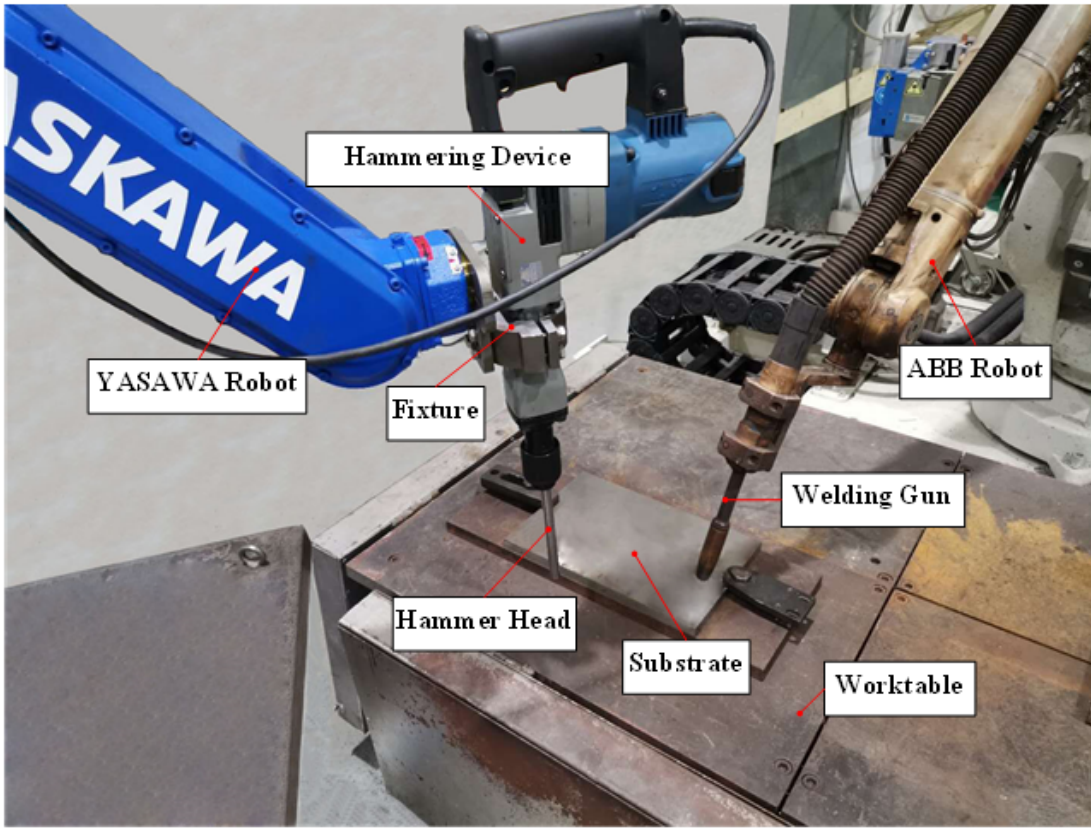


Figure 8

FMF-WAAM experiment system.



(a)

(b)

Figure 9

Deposited layers manufactured by the FMF WAAM process: (a) single-layer single-pass; (b) multi-layer multi-pass

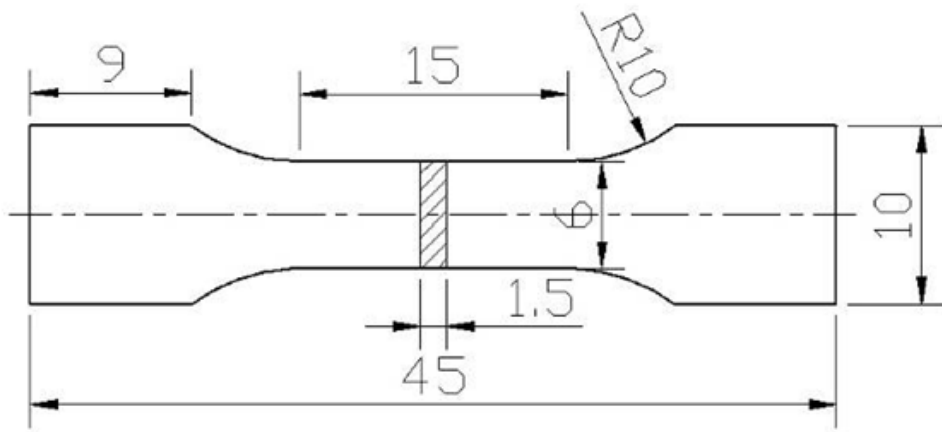
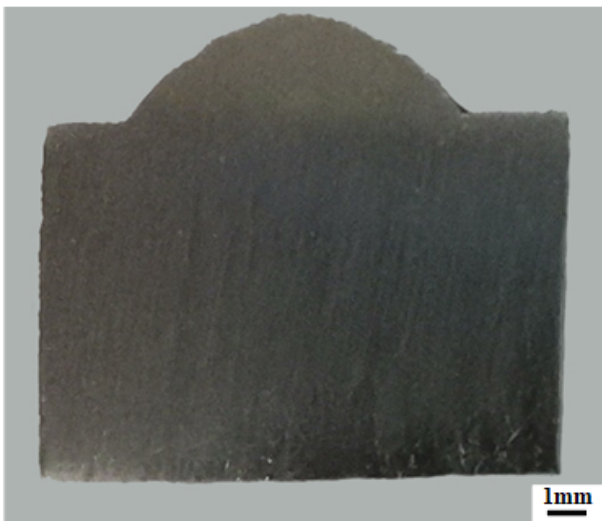
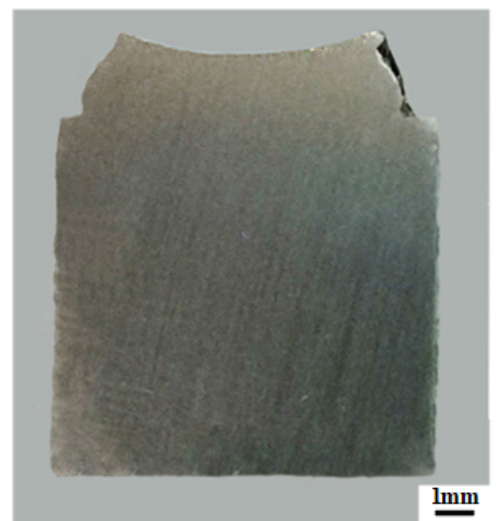


Figure 10

Tensile sample dimensions.



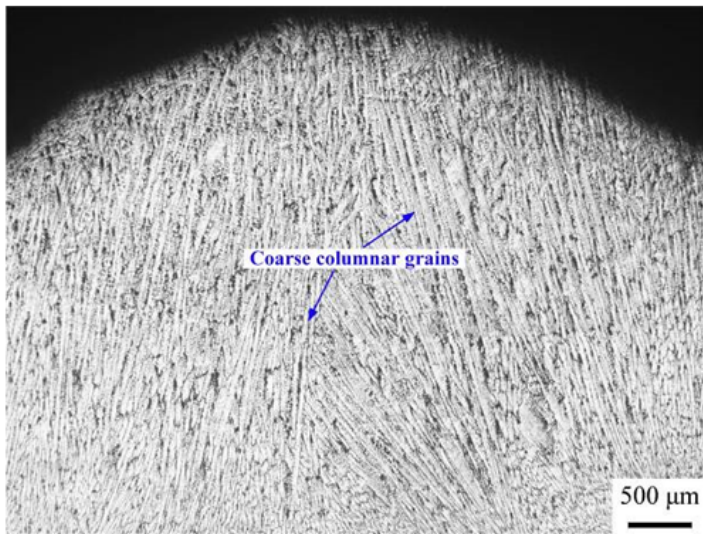
(a)



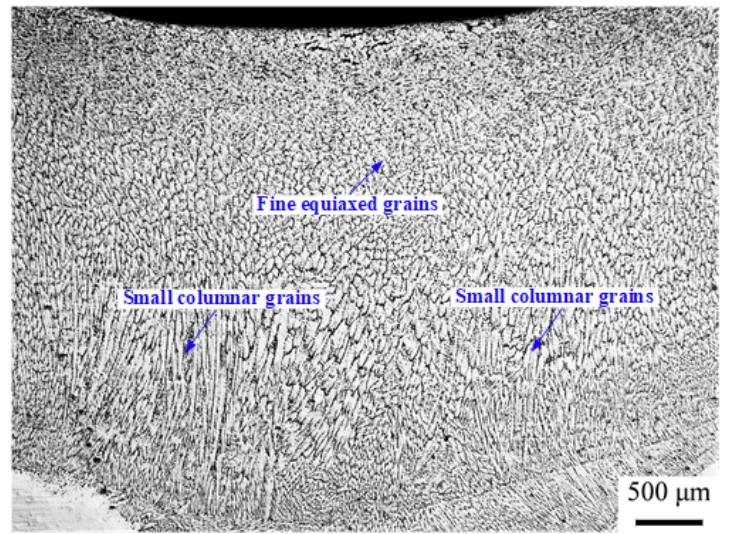
(b)

Figure 11

Cross sections of the single-pass deposited weld:(a) as-deposited; (b) FMF.



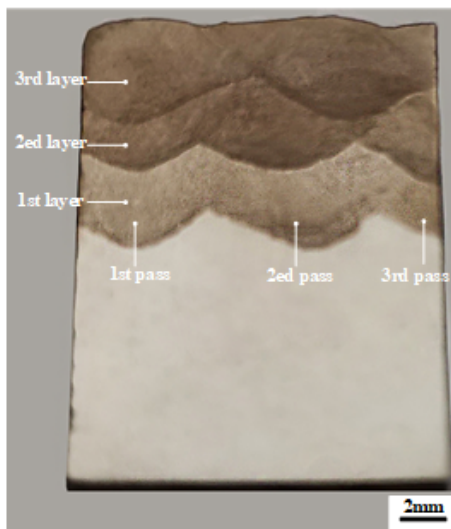
(a)



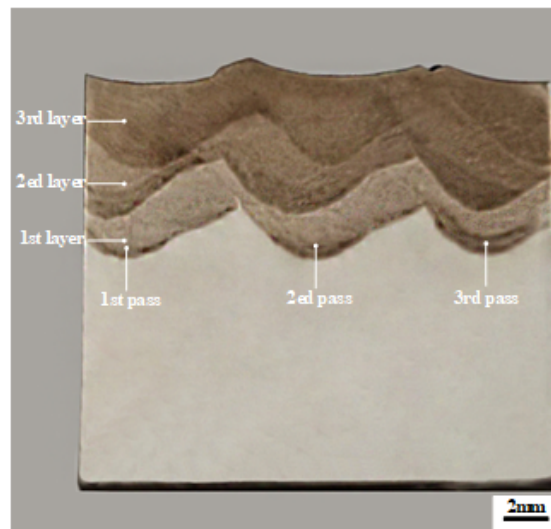
(b)

Figure 12

Metallographic diagrams of cross sections of the single-layer single-pass deposited weld: (a) as-deposited; (b) FMF.



(a)



(b)

Figure 13

Cross sections of the cutted three-layer three-pass deposited layers:(a) as-deposited; (b) FMF.

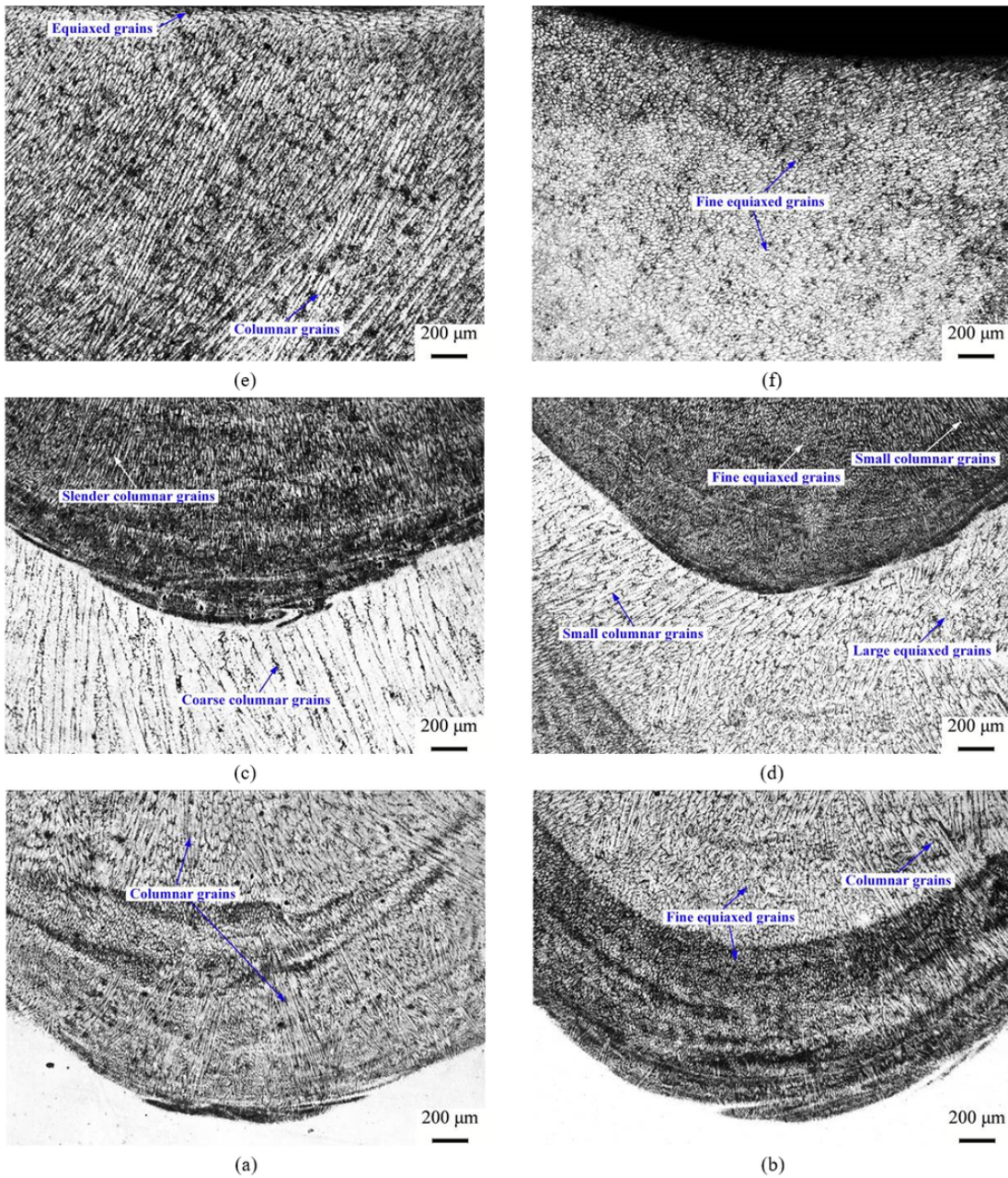
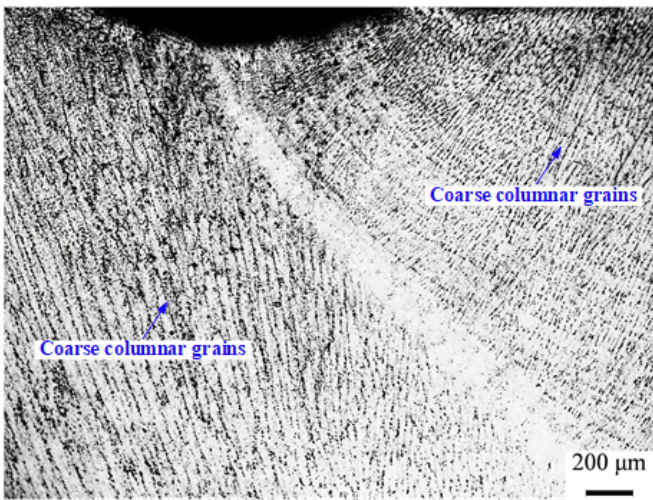
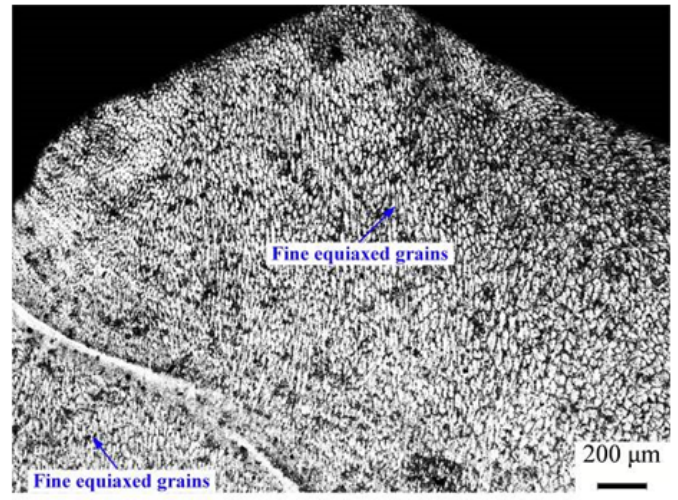


Figure 14

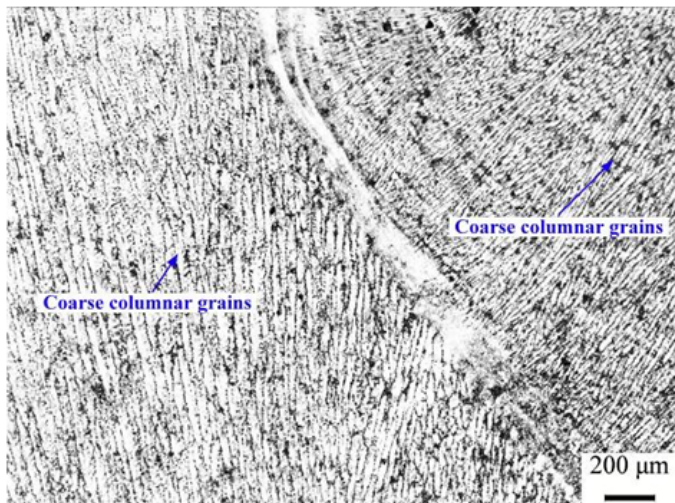
Metallographic diagrams of welds and junctional regions between different welds in different deposited layers: (a) region near the lower edge of the first pass weld in the first deposited layer of the as-deposited; (b) region near the lower edge of the first pass weld in the first deposited layer of the FMF; (c) junctional region between the first pass weld of the first deposited layer and that of the second deposited layer of the as-deposited; (d) junctional region between the first pass weld of the first deposited layer and that of the second deposited layer of the FMF; (e) region near the surface of the first pass weld in the top deposited layer of the as-deposited; (f) region near the surface of the first pass weld in the third deposited layer of the FMF.



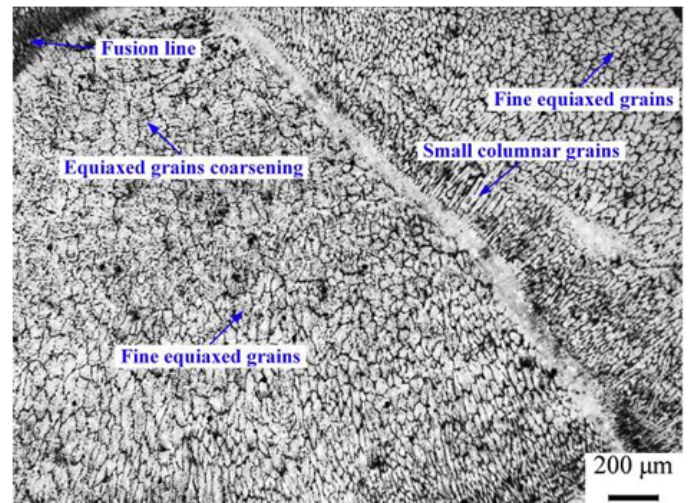
(c)



(d)



(a)



(b)

Figure 15

Metallographic diagrams of the lap bonding regions between different passes in the same deposited layer: (a) lap bonding region between the first pass weld and the second one in the bottom deposited layer of the as-deposited; (b) lap bonding region between the first pass weld and the second one in the bottom deposited layer of the FMF; (c) lap bonding region between the first pass weld and the second one in the top deposited layer of the as-deposited; (d) lap bonding region between the first pass weld and the second one in the top deposited layer of the FMF.

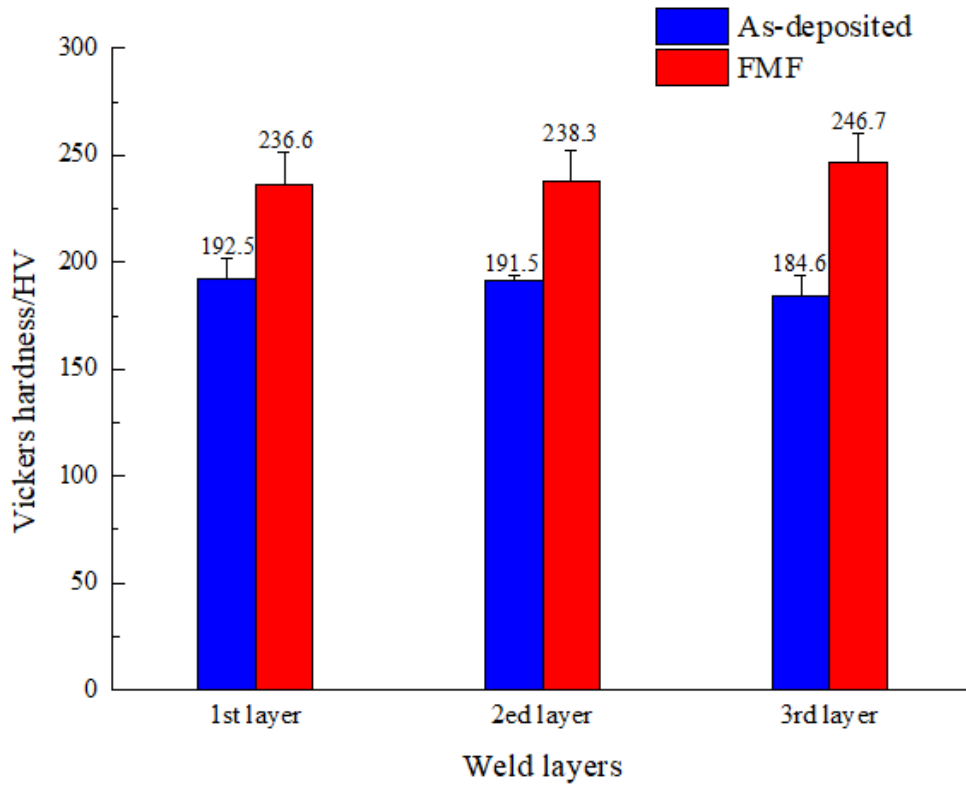
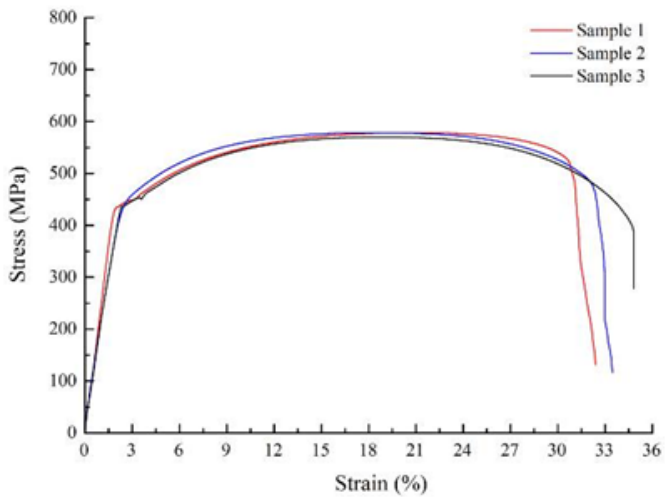
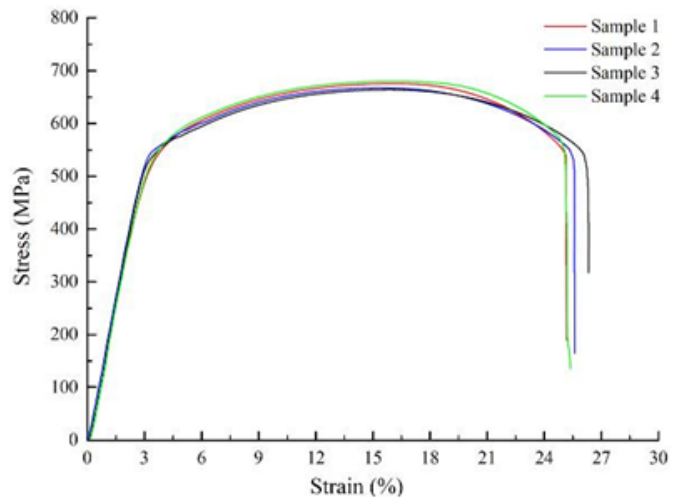


Figure 16

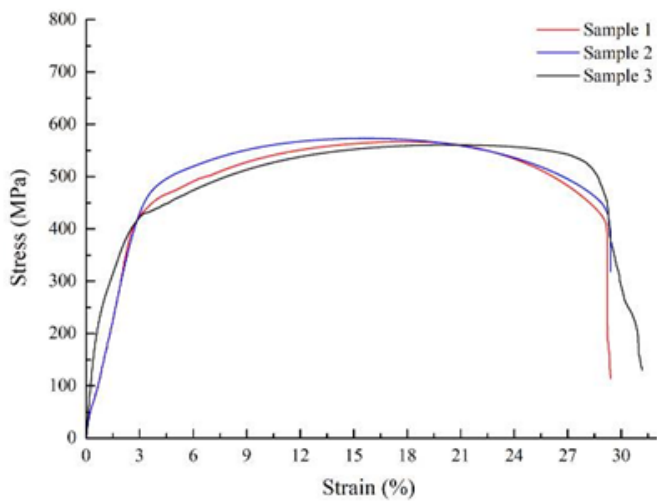
Hardness values of each deposited layer of the as-deposited group and the FMF one.



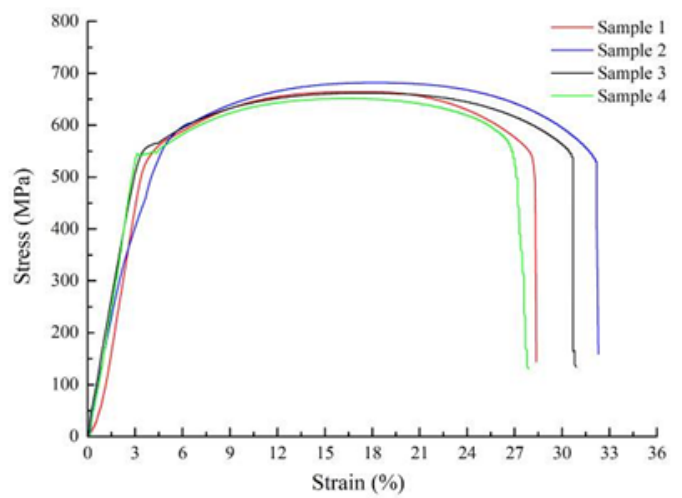
(a)



(b)



(c)



(d)

Figure 17

Stress-strain curves of longitudinal and transverse samples for the as-deposited group and the FMF one: (a) longitudinal samples for the as-deposited; (b) longitudinal samples for the FMF; (c) transverse samples for the as-deposited; (d) transverse samples for the FMF.

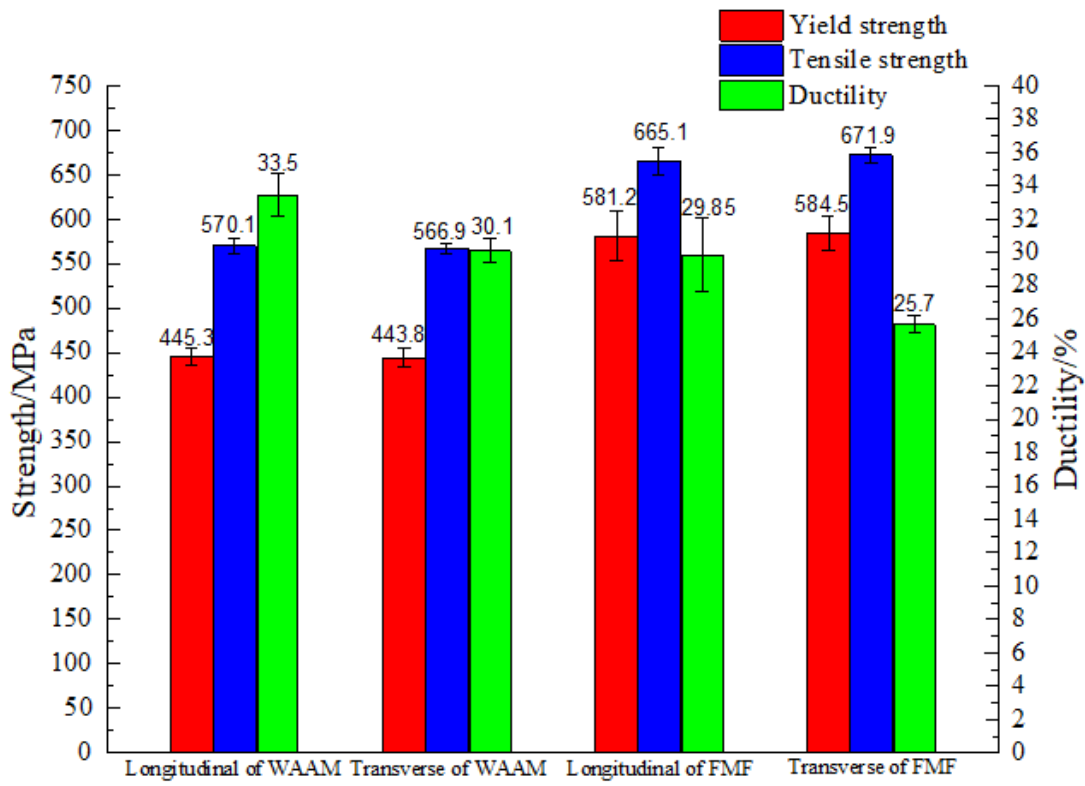


Figure 18

Longitudinal and transverse strength and ductility of the as-deposited group and the FMF one.

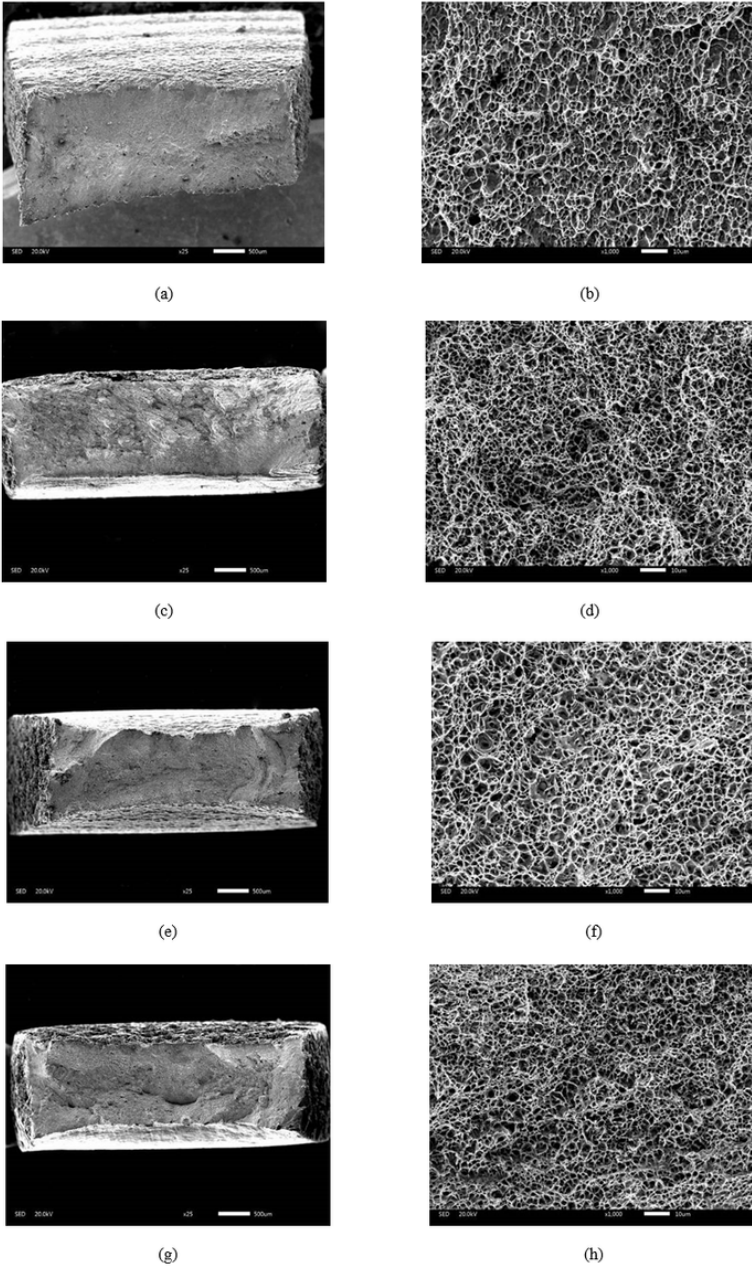


Figure 19

SEM fracture surfaces of the longitudinal and the transverse tensile specimens: (a) (b) longitudinal of the as-deposited; (c) (d) longitudinal of the FMF; (e) (f) transverse of the as-deposited; (g) (h) transverse of the FMF.